Linear Parameter-Varying Control of A Power-Synchronized Grid-Following Inverter

Milad Zarif Mansour, *Graduate Student Member, IEEE,* Mohammad Hasan Ravanji, *Member, IEEE,* Alireza Karimi, *Member, IEEE,* Behrooz Bahrani, *Senior Member, IEEE*

***Abstract*—This paper proposes a Linear Parameter-Varying loop-shaping controller for a power-synchronized grid-following inverter (PSGFLI). This control strategy regulates the inverter output active and reactive power at the terminal instead of the point of connection and does not require a phase-locked loop (PLL) for extracting the voltage phase angle. Hence, the prevalent stability issues exhibited when GFLIs are connected to weak grids are not present, and the proposed PSGFLI control strategy can work under both very weak and strong grid conditions without being prone to instability. In this approach, the controller parameters are functions of the operating point and are changed during the real-time operation such that the closed-loop performance is preserved in all operating points. Furthermore, since the grid impedance is a factor in the design process, a robustness analysis against grid impedance estimation error is conducted, and it is shown that discrepancies in the estimated and real grid impedances are unlikely to make the system unstable. The performance of the proposed control design is validated in MATLAB/PLECS and experiments for both strong and weak grids.**

***Index Terms*—Linear Parameter-Varying, Loop-Shaping, Power Control, Power Synchronized.**

I. Introduction

In recent years, inverter-based resources (IBRs) have gained increasing importance in power systems as a result of their decreasing cost and increasing concerns regarding CO_2 emissions. Hence, their penetration in power grids is rapidly increasing, and conventional synchronous generators are being replaced by them. Despite their advantages, IBRs may face stability and grid synchronization issues due to the shortcomings of the conventional control structures used for this purpose [1].

According to their synchronization strategy, IBRs can be classified into two main groups: 1) grid-following inverters (GFLIs) and 2) grid-forming inverters (GFMIs). Conventional GFLIs employ Phase-Locked Loops (PLLs) for estimating the grid voltage angle, by which they can get synchronized with the grid [2]–[4]. In this type of IBRs, the point of connection (PoC) voltage is used to extract the grid voltage angle, which is in turn needed in a vector current controller [5]–[7]. GFMIs, on the other hand, adjust the phase angle of the PoC voltage by controlling the inverter output active power [8]. In this type of inverter, the active power-frequency droop control is used to synchronize the inverter with the grid [3], [9]–[11]. Additionally, the PoC voltage magnitude is regulated by the inverter based on the output reactive power, in contrast to GFLIs. Note that one major difference between GFLIs and GFMIs is that, contrary to GFLIs, GFMIs can perform in the islanded mode as they form/regulate the PoC voltage. In light of the different control strategies used in these two types of inverters, the stability issues they may have are different.

As the most prevalent IBR control strategy, GFLIs encounter stability issues while integrated into weak grids [12]. Different studies show the main instability motivation is particularly due to the PLL issues in weak grids, which might not have an equilibrium point or have an unstable one [13]–[19]. On the other hand, GFMIs face issues when connected to strong grids as it is challenging to regulate the PoC voltage in such grids [20], [21]. Since GFMIs can be modeled as a first-order system, their transient stability improves compared with GFLIs [22]. Despite that, the droop control loop used for reactive power control can negatively affect the transient stability [23]. In addition, GFMIs can induce oscillations while connected to strong or series compensated grids [21], [24], [25]. Moreover, the output current limiting during a fault occurrence is challenging for this type of IBRs [26]. Additionally, [27] shows that the small-signal stability of virtual synchronous machines (VSMs), as a prevalent GFMI implementation, depends on either the PoC voltage dq-components or the employed impedance of the virtual machine model.

To overcome the stability issues corresponding to the GFLIs and GFMIs, some studies proposed direct power control (DPC) for the IBRs that control the IBRs output active and reactive power directly without having an inner control loop [28], [29]. These methods use a variable switching frequency that causes a wide range of harmonics, and hence, it is not easy to design a filter for them. To conquer this, other DPC methods are proposed that have a constant switching frequency [30]–[34]. Nonetheless, these methods could not eliminate power oscillations either entirely. In addition, [35] proposes a universal control strategy that combines power-synchronization and GFLI schemes to exploit their merits simultaneously. However, this structure still requires a PLL for synchronization and the PoC voltage for its operation. A PLL-less voltage-modulated direct power control (VMDPC) for IBRs is introduced in [36]–[38]. Given the fact that the PLL is eliminated from this control structure, the VMDPC does not have the PLL-related issues that conventional GFLIs suffer from. Nonetheless, this method faces problems while integrated into weak grids due to the necessity of PoC voltage sensing [38]. Also, [39] shows that this approach does not possess any merit compared to conventional PLL-based GFLIs provided the PLL is tuned properly.

To address the shortcomings of the previous methods for controlling grid-following IBRs, [40] proposes a power-synchronized GFLI (PSGFLI) control strategy. This method, similar to the VMDPC, does not use a PLL for grid synchronization. However, unlike the VMDPC, since this method does not require PoC voltage measurement, it is not affected in weak grid conditions, and thus, it can perform in both stiff and weak grids. This method uses the inverter terminal voltage instead of the PoC voltage to control the inverter terminal output power. This control structure is composed of an outer loop that is responsible for controlling the IBR active and reactive power, and generates the frequency and inner loop current references. The current controller employed in this control structure is the conventional vector current controller. Although this method is effective, and the IBR can work under stiff and weak grid conditions, the active and reactive power control design method proposed in [40] is not straightforward since it

uses optimization techniques for control design. Furthermore, the performance depends on the operating point of the system, and the IBR cannot work as a rectifier since the phase margin of the system becomes negative while working as a rectifier unless the controller is modified.

This paper aims to rectify the aforementioned shortcomings of the method proposed in [40]. To this end, a Linear Parameter-Varying (LPV) loop-shaping controller is designed for the proposed IBR control structure, named LPV-PSGFLI. LPV systems are a class of nonlinear systems that have the structure of a linear system whose parameters are a function of some scheduling variables that can be measured in real-time operation [41]. A nonlinear system linearized around some operating points can be represented as an LPV system in which the scheduling variables are the operating point parameters. The LPV systems are linear time-invariant for fixed scheduling variables. An LPV controller is designed such that its parameters are adapted automatically in real-time according to the variation of the operating points. The main benefits of the proposed control design introduced in this paper are

- constant bandwidth for different operating points,
- straightforward control design based on the IBR operating point, and
- inversion and rectification capabilities.

Additionally, this study provides a robustness analysis of the proposed controller against the grid impedance estimation error. It is shown that while the order of the system increases, in case the grid impedance is not accurately estimated, the system instability is unlikely. Note that this study does not employ a fault-ride through (FRT) scheme during faults. The reason is highlighting the capabilities of the proposed controller during and after faults. However, FRT schemes are used in practice to help inverters remain synchronized with the grid during faults, and similarly to other GFLIs, FRT techniques can be implemented on the control strategy proposed in this article.

The rest of this paper is organized as follows. Section II discusses the VMDPC and PSGFLI. Section III describes the proposed LPV loop-shaping control design and analyzes the robustness of the system with respect to discrepancies between the grid estimated and real impedances. The performance of the proposed method is evaluated in Section IV. Finally, the conclusions are presented in Section V.

II. Power-Synchronized Grid-Following Inverter Control

To have a system that can work in all grid strengths, a novel power-synchronized control strategy for GFLIs is proposed in [40]. The block diagram of this control strategy is shown in Fig. 1. It is worth mentioning that, as shown in [40], and since the PoC voltage is not used/regulated in this control strategy, using L or LCL filters does not impact the controller performance; hence, without loss of generality, an L filter is employed in this study. If an LCL filter is used, the internal current controller needs to be designed such that it damps the resonance created by the LCL filter [7], [42].

The advantage of the control strategy of [40] compared with conventional GFLIs is that no PLL is used in this method, and hence, the related stability issue in weak grids is not exhibited. Additionally, this control strategy does not rely on sensing/controlling PoC voltage. Thus, this method does not present the stability deterioration related to the VMDPC reported in [38], which is due to the affected PoC voltage. Ref. [40] shows that while this method can work in very weak grids, the VMDPC fails; unless the system time constant decreases significantly, making the system much slower.

Ref. [40] assumes that the rotating reference frame is aligned with the inverter output current, which makes i_{q}=0 A. Thus, the inverter output current and voltage can be written as

$$i_{\mathrm{dq}} = I_{\mathrm{d}} + j0 \;\text{ and }\; v_{t,\mathrm{dq}} = V_t\cos\delta + jV_t\sin\delta. \tag{1}$$

In (1), δ is the angle between the inverter output voltage and current, I_{d} is the d-component of the inverter output current, and V_t is the amplitude of the inverter output phase-to-neutral voltage. Moreover, the inverter apparent output power is

$$P + jQ = \frac{3}{2}\big(V_t I_{\mathrm{d}}\cos\delta + jV_t I_{\mathrm{d}}\sin\delta\big). \tag{2}$$

Supposing that there are small perturbations in δ and I_{d}, i.e., δ=δ_0+$\Delta\delta$ and I_{d}=$I_{\mathrm{d},0}$+ΔI_{d}, the small-signal model of the system can be derived as [40]

$$\begin{pmatrix}\Delta P\\ \Delta Q\end{pmatrix} = \underbrace{\begin{pmatrix}\frac{3V_t I_{\mathrm{d},0}\sin\delta_0}{2s}H & \frac{3V_t\cos\delta_0}{2(\tau s+1)}H\\ -\frac{3V_t I_{\mathrm{d},0}\cos\delta_0}{2s}H & \frac{3V_t\sin\delta_0}{2(\tau s+1)}H\end{pmatrix}}_{\mathbf{G}}\begin{pmatrix}\Delta\omega\\ \Delta I_{\mathrm{d,ref}}\end{pmatrix}, \tag{3}$$

in which $\mathbf{G}$ is the system transfer function matrix, H is the input low-pass filter and will be neglected from now on, $\frac{1}{\tau s+1}$ represents the current controller assuming that the grid impedance is known, P and Q are inverter output active and reactive power, δ_0 is the angle between inverter voltage and current at the operating point, $I_{\mathrm{d},0}$ is the inverter output current d-component, ω is the estimated angular frequency of the grid by the controller, and finally, $I_{\mathrm{d,ref}}$ is the inverter output current d-component reference. Note that assuming that the zero of the current controller PI and the pole imposed by the grid impedance to the system cancel each other, the transfer function of the closed current control loop can be written as $\frac{1}{\tau s+1}$ [7].

An outer-loop control schematic for regulating the output P and Q is proposed in [40], which is shown in Fig. 2. In this figure, $K_{11}(s)$ through $K_{22}(s)$ are Proportional-Integral (PI) compensators. Although the control strategy proposed in [40] is capable of working in very weak and very strong systems, its control design method is complex. First, it uses optimization techniques to design the active and reactive power PI controllers. Additionally, using the PI controllers proposed in [40], the system cannot work as a rectifier since the phase margin of the system becomes negative, making the system unstable. Finally, using the control design method in [40], the bandwidth of the system depends on the operating point of the system, i.e., unless the system operating point is about the operating point the controller is designed for, the system becomes slower or faster than desired.

Hence, in the following, an alternative controller that addresses the aforementioned shortcomings of the proposed controller in [40] is devised, which is easy to design, has a fixed bandwidth in different operating points, and can work as an inverter and rectifier.

III. LPV Loop-shaping Control Design

As seen from (3), the system under study is a MIMO system; hence, a 2×2 controller must be designed to guarantee stability. To do so, in this study, an LPV loop-shaping controller is designed such that it addresses the drawbacks of the controller designed in [40]. To design the LPV controller, a vector of scheduling parameters should be chosen, which is selected as μ=$[I_{\mathrm{d},0}, \delta_0]^T$.

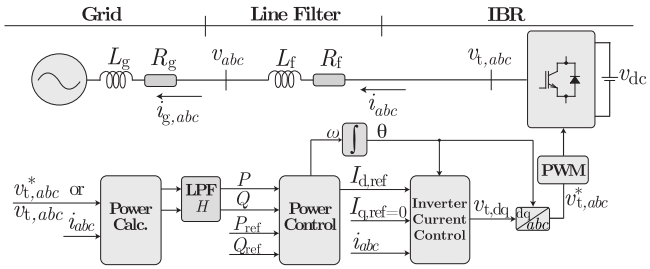

Fig. 1. Power-synchronized GFLI and its control structure.

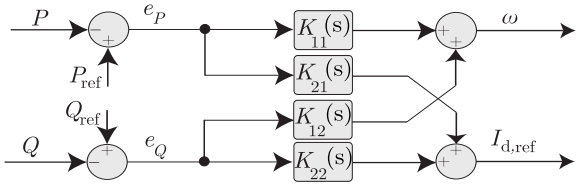

Fig. 2. The block diagram of the proposed power controller.

TABLE I
THE PARAMETERS OF THE STUDY SYSTEM OF FIG. 1.

Quantity	Value	Comment
L_f	95 μH	Inverter Filter Inductance
R_f	0.01 Ω	Series Resistance of L_f
S_{base}	5 MVA	Inverter Rated Power
v_g	690 V	Grid Line-to-Neutral Voltage (rms)
v_{dc}	3000 V	DC Bus Voltage
f_{sw}	5 kHz	PWM Carrier Frequency
f	50 Hz	System Nominal Frequency
f_{filt}	200 Hz	Power Measurement LPF Bandwidth

Hence, the designed controller and the system both are functions of the vector μ.

Supposing that the desired open-loop transfer function matrix of the system, $\mathbf{L_D}$, is chosen as

$$\mathbf{L_D} = \begin{pmatrix} k_p/s & 0 \\ 0 & k_p/s \end{pmatrix}, \tag{4}$$

and assuming that $\mathbf{K}(\mu)$ is the designed 2×2 controller, the open-loop transfer function can be written as

$$\mathbf{L}(\mu) = \mathbf{G}(\mu) \times \mathbf{K}(\mu). \tag{5}$$

In case the open-loop transfer function is equal to the desired transfer function introduced in (4),

$$\mathbf{K}(\mu) = \mathbf{G}^{-1}(\mu) \times \mathbf{L_D}. \tag{6}$$

Note that the chosen $\mathbf{L_D}$ guarantees stability since the closed-loop transfer functions on the diagonal entries become $\frac{K_p}{s+K_p}$, which is a stable transfer function. Additionally, $\mathbf{L_D}$ provides a decoupled system as its off-diagonal elements are zero. To find the controller matrix, $\mathbf{K}(\mu)$, the inverse of $\mathbf{G}(\mu)$ can be derived as

$$\mathbf{G}^{-1}(\mu) = \begin{pmatrix} \frac{2s\sin\delta_0}{3V_t I_{d,0}} & -\frac{2s\cos\delta_0}{3V_t I_{d,0}} \\ \frac{2(\tau s+1)\cos\delta_0}{3V_t} & \frac{2(\tau s+1)\sin\delta_0}{3V_t} \end{pmatrix}. \tag{7}$$

By replacing (7) in (6), the controller matrix becomes

$$\mathbf{K}(\mu) = \begin{pmatrix} k_p\frac{2\sin\delta_0}{3V_t I_{d,0}} & -k_p\frac{2\cos\delta_0}{3V_t I_{d,0}} \\ k_p\frac{2(\tau s+1)\cos\delta_0}{3V_t s} & k_p\frac{2(\tau s+1)\sin\delta_0}{3V_t s} \end{pmatrix}. \tag{8}$$

Keeping in mind that i_q=0 A, the apparent power can be written as

$$S_t = \frac{3}{2} V_t I_d. \tag{9}$$

By replacing (9) in (8), the designed controller can be reformulated as

$$\mathbf{K}(\mu) = \begin{pmatrix} k_p\frac{\sin\delta_0}{S_t} & -k_p\frac{\cos\delta_0}{S_t} \\ k_p\frac{(\tau s+1)I_{d,0}\cos\delta_0}{s\times S_t} & k_p\frac{(\tau s+1)I_{d,0}\sin\delta_0}{s\times S_t} \end{pmatrix}, \tag{10}$$

in which S_t is the inverter output apparent power and can be written as $S_t=\sqrt{P^2+Q^2}$, $\delta_0=\tan^{-1}\frac{Q}{P}$, and $I_{d,0}$ is the inverter output current peak value, which can be updated in the controller shown in (10) via real-time measurements. It is worth mentioning that by choosing the desired open-loop transfer function as shown in (4), the closed-loop transfer function becomes

$$\mathbf{G_{cl}} = \begin{pmatrix} \frac{k_p}{s+k_p} & 0 \\ 0 & \frac{k_p}{s+k_p} \end{pmatrix} = \begin{pmatrix} \frac{1}{Ts+1} & 0 \\ 0 & \frac{1}{Ts+1} \end{pmatrix}, \tag{11}$$

in which $T=\frac{1}{k_p}$ is the system time constant. Hence, the bandwidth of the system dynamic response can be directly adjusted by setting k_p.

The main advantage of the controller proposed in (10) compared to the control design method in [40] is that (10) is easy to design and does not require system identification and/or solving an optimization-based loop-shaping problem since it provides a parametric loop-shaping controller. In addition, unlike the method proposed in [40], (10) schedules its gains based on the system operating point. Hence, in contrast to [40], the system bandwidth is not changed by changing the IBR operating point. Finally, this controller allows the system to perform bidirectionally, i.e., in inverter and rectifier modes. The reason is that regardless of the power direction, the system open-loop transfer function is $\mathbf{L_D}$ using the proposed LPV controller, which is a stable system. However, the controller designed in [40] does not work in rectifier mode.

As mentioned above, the transfer function in (3) assumes that the grid impedance is known, and the current controller can be simplified to a first-order system with a time constant τ. This transfer function is used to design the controller proposed in (8). Although there are many approaches for accurate impedance estimation in the literature [43], [44], errors in the grid impedance estimation can occur in the system; thus, a robustness analysis against impedance estimation errors is needed.

A. Robustness Analysis Against Grid Impedance Estimation Error

Supposing that the grid inductance and resistance are known, the PI controller employed in the current controller can be devised such that it has a zero at $Ls+R$, where L is the grid inductance, and R is the grid resistance; hence, the closed-loop transfer function of the current controller can be written as $\frac{K_{p,cc}}{s+K_{p,cc}}$, or alternatively, $\frac{1}{\tau_1 s+1}$, where $\frac{1}{K_{p,cc}}=\tau_1$. If the exact values of the grid impedance and resistance are not known, the open-loop transfer function corresponding to the current controller becomes

$$G_{o,cc}(s) = K_{p,cc} \times \frac{\hat{L}s+\hat{R}}{s} \times \frac{1}{Ls+R}, \tag{12}$$

where $\hat{L}$ and $\hat{R}$ are the estimated grid inductance and resistance and can be written as $\hat{L}=a_1\times L$ and $\hat{R}=a_2\times R$, respectively. To analytically study the estimation errors impact on the system stability and for the sake of simplicity, it is assumed that $a_1=a_2=a$. However, in the provided numerical analysis, different errors are considered, i.e., $a_1\neq a_2$.

Based on the assumption in the analytical study, the open-loop zero and pole in (12) still cancel each other; however,

the estimation error is reflected in the open-loop gain, making it $a{\times}K_{p,\mathrm{cc}}$. Supposing $\frac{1}{a\times K_{p,\mathrm{cc}}}{=}\tau_2$, the transfer function of the closed current control loop can be written as

$$G_{\mathrm{cc}}(s)=\frac{1}{\tau_2 s+1}. \tag{13}$$

Replacing (13) in (3) results in

$$\mathbf{G}(\mu)=\begin{pmatrix}\frac{3V_t I_{\mathrm{d},0}\sin\delta_0}{2s} & \frac{3V_t\cos\delta_0}{2(\tau_2 s+1)}\\ -\frac{3V_t I_{\mathrm{d},0}\cos\delta_0}{2s} & \frac{3V_t\sin\delta_0}{2(\tau_2 s+1)}\end{pmatrix}. \tag{14}$$

By replacing (8) and (14) in (5), the open-loop transfer function of the system with the estimation error can be written as

$$\begin{aligned}\mathbf{L}(\mu)&=\mathbf{G}(\mu)\times\mathbf{K}(\mu)\\
&=\begin{pmatrix}\frac{3V_t I_{\mathrm{d},0}\sin\delta_0}{2s} & \frac{3V_t\cos\delta_0}{2(\tau_2 s+1)}\\ -\frac{3V_t I_{\mathrm{d},0}\cos\delta_0}{2s} & \frac{3V_t\sin\delta_0}{2(\tau_2 s+1)}\end{pmatrix}\begin{pmatrix}\frac{2s\sin\delta_0}{3V_t I_{\mathrm{d},0}} & -\frac{2s\cos\delta_0}{3V_t I_{\mathrm{d},0}}\\ \frac{2(\tau_1 s+1)\cos\delta_0}{3V_t} & \frac{2(\tau_1 s+1)\sin\delta_0}{3V_t}\end{pmatrix}\\
&=\begin{pmatrix}\frac{k_p\sin{\delta_0}^2}{s}+\frac{k_p\cos{\delta_0}^2}{s}\times\frac{\tau_1 s+1}{\tau_2 s+1} & -\frac{k_p\sin 2\delta_0}{2s}+\frac{k_p\sin 2\delta_0}{2s}\times\frac{\tau_1 s+1}{\tau_2 s+1}\\ \frac{k_p\sin 2\delta_0}{2s}-\frac{k_p\sin 2\delta_0}{2s}\times\frac{\tau_1 s+1}{\tau_2 s+1} & \frac{k_p\cos{\delta_0}^2}{s}+\frac{k_p\sin{\delta_0}^2}{s}\times\frac{\tau_1 s+1}{\tau_2 s+1}\end{pmatrix}\\
&=\begin{pmatrix}\frac{k_1}{s}+\frac{k_2}{s}\times\frac{\tau_1 s+1}{\tau_2 s+1} & -\frac{k_3}{s}+\frac{k_3}{s}\times\frac{\tau_1 s+1}{\tau_2 s+1}\\ \frac{k_3}{s}-\frac{k_3}{s}\times\frac{\tau_1 s+1}{\tau_2 s+1} & \frac{k_2}{s}+\frac{k_1}{s}\times\frac{\tau_1 s+1}{\tau_2 s+1}\end{pmatrix}\\
&=\begin{pmatrix}\frac{k_1(\tau_2 s+1)+k_2(\tau_1 s+1)}{s(\tau_2 s+1)} & \frac{-k_3(\tau_2 s+1)+k_3(\tau_1 s+1)}{s(\tau_2 s+1)}\\ \frac{k_3(\tau_2 s+1)-k_3(\tau_1 s+1)}{s(\tau_2 s+1)} & \frac{k_2(\tau_2 s+1)+k_1(\tau_1 s+1)}{s(\tau_2 s+1)}\end{pmatrix},\end{aligned} \tag{15}$$

in which

$$k_1=k_p\sin^2\delta_0\quad;\quad k_2=k_p\cos^2\delta_0\quad;\quad k_3=k_p\frac{\sin 2\delta_0}{2}. \tag{16}$$

To evaluate the stability of the system, the poles of the closed-loop transfer function must be found. To do so, the closed-loop transfer function can be written as

$$\hat{\mathbf{G}}_{\mathbf{cl}}(\mu)=\mathbf{L}(\mu)\times(\mathbf{L}(\mu)+\mathbf{I})^{-1}. \tag{17}$$

To find the closed-loop system poles, the characteristic equation of each entry in (17) should be found. Supposing that the system is minimal (no pole-zero cancellation occurs in the system), it can be shown that each entry characteristic equation, $\Delta(s)$, is the numerator of $\det(\mathbf{L}(\mu)+\mathbf{I})$. Hence, to have a stable system, the roots of $\Delta(s)$ should be negative. The characteristic equation can be found as

$$\begin{aligned}\Delta(s)=&\overbrace{(k_1k_2+k_3^2)}^{A}(\tau_2 s+1)^2+\overbrace{(k_1k_2+k_3^2)}^{A}(\tau_1 s+1)^2\\
&+\overbrace{(k_1^2+k_2^2-2k_3^2)}^{B}(\tau_1 s+1)(\tau_2 s+1)\\
&+\overbrace{(k_1+k_2)}^{C}s(\tau_2 s+1)\\
&+\overbrace{(k_1+k_2)}^{C}s(\tau_1 s+1)(\tau_2 s+1)+s^2(\tau_2 s+1).\end{aligned} \tag{18}$$

Thus, $\Delta(s)$ can be rewritten as

$$\begin{aligned}\Delta(s)=&\tau_2^2 s^4+(2\tau_2+C\tau_1\tau_2)s^3\\
&+\{A(\tau_2^2+\tau_1^2)+(B+C)(\tau_1+\tau_2)+C\tau_2+1\}s^2\\
&+\{2A(\tau_1+\tau_2)+B(\tau_1+\tau_2)+2C\}s+2A+B.\end{aligned} \tag{19}$$

To have a stable system, the roots of (19) must be negative. To find the stability condition, the Routh-Hurwitz criterion is employed. Based on this criterion, to have a stable system,

$$\begin{aligned}&1)2A+B>0,\\
&2)2\tau_2+C\tau_1\tau_2>0,\text{ and}\\
&3)\{(2\tau_2+C\tau_1\tau_2)[A(\tau_1^2+\tau_2^2)+(B+C)(\tau_1+\tau_2)+C\tau_2+1]\\
&-\tau_2^2[2A(\tau_1+\tau_2)+B(\tau_1+\tau_2)+2C]\}\\
&\times\{2A(\tau_1+\tau_2)+B(\tau_1+\tau_2)+2C\}\\
&-(2\tau_2+C\tau_1\tau_2)^2(2A+B)>0.\end{aligned} \tag{20}$$

The first condition in (20) is always valid since $2A{+}B{=}(k_1{+}k_2)^2$. Additionally, since $C{=}k_1{+}k_2{>}0$, and considering that τ_1 and τ_2 are positive values, the second condition in (20) is always valid. To evaluate the last condition, it should be noted that the current controller time constant (τ) is about a couple of ms; hence, the terms containing higher order of τs, i.e., their multiplication or higher power ratings, can be neglected. By doing so, the third condition can be simplified to $4C\tau_2$, which is always positive. Therefore, it can be concluded that if the inductance and resistance estimation error percentages are the same, the system remains stable, while some dynamics are added to the system.

In a general case, when the inductance and resistance estimations have random and not necessarily equal errors, the pole and zero in (12) do not cancel each other, and hence, neglecting the coupling between the current d and q-components, the transfer function of the closed current control loop becomes

$$G_{\mathrm{cc_{general}}}(s)=K_{p,\mathrm{cc}}\frac{\hat{L}s+\hat{R}}{Ls^2+(R+K_{p,\mathrm{cc}}\hat{L})s+K_{p,\mathrm{cc}}\hat{R}}, \tag{21}$$

and the system transfer function becomes

$$\mathbf{G}(\mu)=\begin{pmatrix}\frac{3V_t I_{\mathrm{d},0}\sin\delta_0}{2s} & \frac{3V_t\cos\delta_0}{2}G_{\mathrm{cc_{general}}}(s)\\ -\frac{3V_t I_{\mathrm{d},0}\cos\delta_0}{2s} & \frac{3V_t\sin\delta_0}{2}G_{\mathrm{cc_{general}}}(s)\end{pmatrix}. \tag{22}$$

Since the system order is increased if random errors are assumed for the estimated grid inductance and resistance, making it challenging to analytically evaluate the robustness, a numerical robustness analysis of the system introduced in Table I with the transfer function shown in (22) and the controller shown in (10) is performed. In this analysis, it is assumed that the resistance estimation error is 10%, and the inductance estimation error varies from 5% to 95% with 5% steps. As discussed, the closed-loop system poles are the characteristic equation roots, $\Delta(s)$. Therefore, to assess the stability, the $\Delta(s)$ roots are shown in Fig. 3. The arrows show the estimation error increase. It is seen that the overall closed-loop system remains stable despite the different estimation errors resistance and inductance have.

It should be noted that the presence of errors in the inductance and resistance estimations adds more poles and zeros to the closed-loop transfer function, and hence, some new dynamics will be added to the system; nonetheless, it is not likely that these estimation errors threat the system stability.

B. Grid Frequency Deviation Impact on the Active and Reactive Power Steady-State Errors

One of the disturbances that may occur in power systems is the grid frequency deviation. Hence, the ability of the IBR to remain synchronized with the grid in the presence of frequency changes must be evaluated. Since based on Fig. 2, $\Delta\omega{=}k_{11}e_P{+}k_{12}e_Q$,

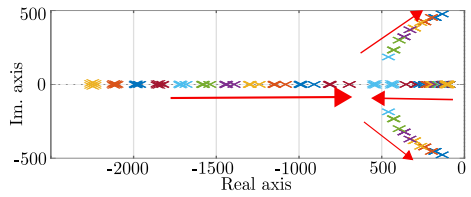

Fig. 3. The characteristic equation roots when the resistance estimation error is 10% and the inductance estimation error varies from 5% to 95%.

and the estimated frequency by the controller that keeps the IBR synchronized to the grid is $\omega{=}\omega_0{+}\Delta\omega$, $\Delta\omega$ is nonzero in the presence of a grid frequency deviation. In case the desired open-loop transfer function is chosen as (4), which results in having k_{11} and k_{12} as two gains, e_p and e_Q become nonzero in the steady-state. In other words, having k_{11} and k_{12} as two gains creates a droop-like relationship between the active and reactive power with the frequency. To calculate the amount of the steady-state errors, using (8), one can write

$$\Delta\omega = \frac{2k_p}{3V_{\mathrm{t}}I_{\mathrm{d,0}}}\big(\sin\delta_0 \times e_P + \cos\delta_0 \times e_Q\big). \tag{23}$$

Also, since k_{21} and k_{22} have an integrator, to have the system stable, the total error signal given to the integrator must be zero in the steady-state, i.e.,

$$0 = \frac{2k_p}{3V_{\mathrm{t}}}\big(\cos\delta_0 \times e_P + \sin\delta_0 \times e_Q\big), \tag{24}$$

which results in

$$e_P = -\tan\delta_0 \times e_Q. \tag{25}$$

By substituting for e_p from (25) in (23),

$$\frac{3V_{\mathrm{t}}I_{\mathrm{d,0}}}{2k_p}\Delta\omega = \overbrace{\Big(\frac{-\sin^2\delta_0}{\cos\delta_0} - \sin\delta_0\Big)}^{D} e_Q, \tag{26}$$

and hence,

$$\frac{3V_{\mathrm{t}}I_{\mathrm{d,0}}}{2k_pD}\Delta\omega = e_Q. \tag{27}$$

By substituting for e_Q from (27) in (25), e_P can be calculated. As expected, it is observed that the injected active and reactive power have steady-state error in the presence of grid frequency deviation. In case the steady-state error is not tolerable, an upper-level controller, such as a governor, can adjust the active and reactive power references. Alternatively, a higher-order open-loop transfer function matrix that has at least two integrators can be used.

IV. Performance Evaluation

To assess the performance of the proposed controller, the system shown in Fig. 1 is simulated in Matlab/PLECS. Furthermore, the performance of the designed controller is validated using an experimental setup based on Imperix B-Box Controller and Regatron AC Power Supply. In the simulation tests, the controller capability for coping with active and reactive power set-point changes, bidirectional performance, phase jump, and fault occurrence is validated under weak and strong grid conditions. In addition, the experimental setup is employed to validate the ability of the controller to cope with active and reactive power set-point changes.

A. Simulation Results

To evaluate the performance of the proposed controller, different tests are conducted in Matlab/PLECS when the system shown in Fig. 1 and with the parameters in Table I is subjected to faults, grid phase jumps, and set-point changes both for strong and weak grids.

1) Strong grid (SCR=17): In this part, the grid inductance and resistance are chosen as $L_{\mathrm{g}}{=}51\ \mu H$ and $R_{\mathrm{g}}{=}5.4\ m\Omega$, respectively, making SCR=17. Also, the PI controller employed in the current controller is $2500{\times}\frac{146{\times}10^{-6}s{+}0.0154}{s}$, making the current controller a first-order system with $\tau{=}0.0004$ s. Besides, k_p is chosen equal to 100, causing a 10 ms overall time constant. Initially, the converter injects 1 MW and 1 MVAR of active and reactive power, respectively. At $t{=}0.05$ s, the active power set-point is changed to 2 MW. At $t{=}0.15$ s, the reactive power set-point steps up to 4 MVAR, while the active power remains unchanged. At $t{=}0.25$ s, the power factor is changed from 0.44 to 0.9, changing the active and reactive power set-points to 4 MW and 2 MVAR, respectively. Finally, at $t{=}0.35$ s, the converter active power set-point is changed to -2 MW, making the converter to work as a rectifier. Fig. 4 depicts the simulation results of this system. Fig. 4(a) shows the three-phase output current, Fig. 4(b) is the converter filter output line-to-neutral three-phase voltage, Fig. 4(c) is d and q-components of the converter output current, Fig. 4(d) is d and q-components of the converter terminal voltage, Fig. 4(e) depicts the output active and reactive power, and finally, Fig. 4(f) shows the angular frequency generated by the controller. It is seen that the controller tracks the reference active and reactive power with zero steady-state error, the time constant of the system is about 10 ms, and the converter can perform as an inverter and rectifier, as expected. Note that the angular frequency shown in Fig. 4(f) is not the grid frequency. It is an internal variable of the inverter, which can be different from the frequency of the grid during transients.

Also, Fig. 5 shows the simulation results of the system upon a fault occurrence and phase jump. Initially, the converter injects $P{=}4$ MW and $Q{=}2$ MVAR into the grid. At $t{=}0.05$ s, a 100 ms three-phase fault making the grid voltage 0.2 pu occurs in the system. It is seen that the injected power is recovered since, based on the physical attributes of the system, the reference active power does not exceed the line power transmission limit. At $t{=}0.15$ s, the fault is cleared, and the grid voltage is recovered. It is seen that the controller copes with the fault clearance. Additionally, at $t{=}0.25$ s, a 20° phase jump occurs at the grid side voltage. It is seen that the system can maintain stability and inject the reference active and reactive power into the grid after the phase jump occurrence.

2) Weak grid (SCR=1.2): In this part, the grid inductance and resistance are chosen as $L_{\mathrm{g}}{=}680\ \mu H$ and $R_{\mathrm{g}}{=}72\ m\Omega$, respectively, making SCR=1.2. Also, the PI controller employed in the current controller is $2500{\times}\frac{770{\times}10^{-6}s{+}0.082}{s}$, making the current controller a first-order system with $\tau{=}0.0004$ s. Similar to the previous test, k_p is chosen equal to 100, causing a 10 ms overall time constant. Initially, the converter injects 1 MW and 1 MVAR of active and reactive power, respectively. At $t{=}0.05$ s, the active power set-point is changed to 2 MW. At $t{=}0.15$ s, the reactive power set-point steps up to 4 MVAR, while the active power remains unchanged. At $t{=}0.25$ s, the power factor is changed from 0.44 to 0.9, changing the active and reactive power set-points to 4 MW and 2 MVAR, respectively. Finally, at $t{=}0.35$ s, the converter active power set-point is changed to -2 MW, making the

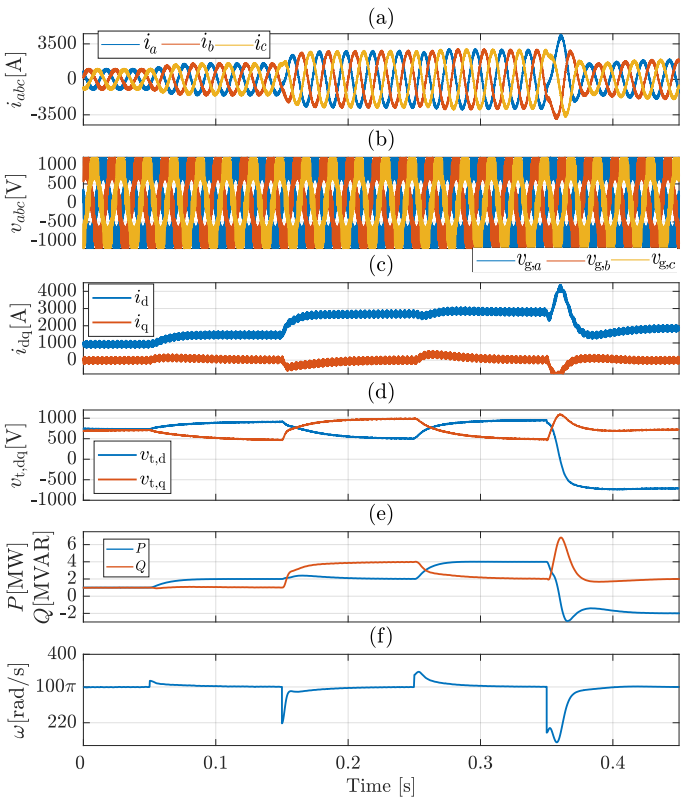

Fig. 4. The simulation results of the system with SCR=17 upon various active and reactive power references change: a) the three-phase grid currents (i_{abc}), b) the converter filter output three-phase line-to-neutral voltage, c) the dq-components of the grid current (i_{dq}), d) the dq-components of the terminal voltage ($v_{t,dq}$), e) the injected active and reactive power into the grid, and f) the estimated angular frequency generated by the controller.

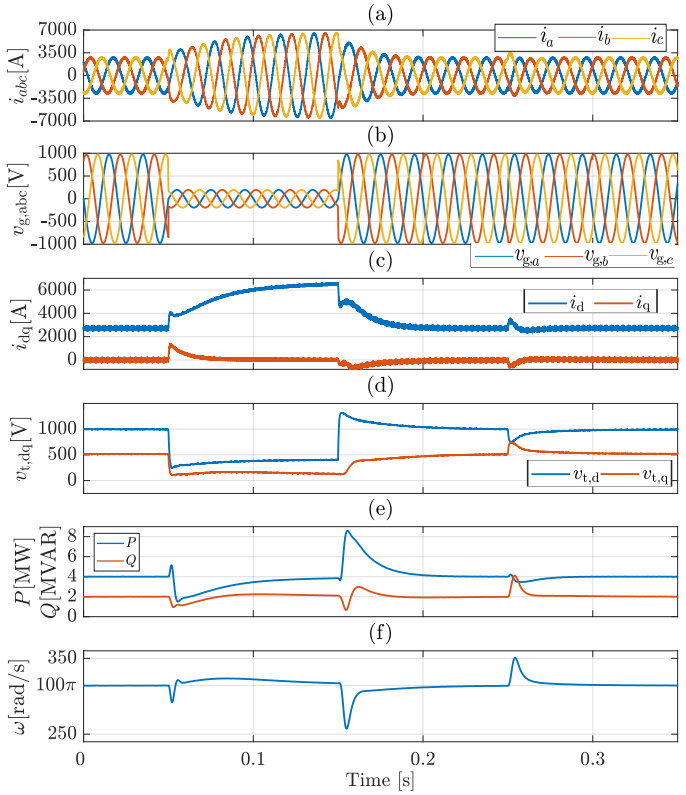

Fig. 5. The simulation results of the system with SCR=17 upon a three-phase fault and grid voltage phase jump occurrence: a) the three-phase grid currents (i_{abc}), b) the grid three-phase line-to-neutral voltage, c) the dq-components of the grid current (i_{dq}), d) the dq-components of the terminal voltage ($v_{t,dq}$), e) the injected active and reactive power into the grid, and f) the estimated angular frequency generated by the controller.

converter to work as a rectifier. Fig. 6 depicts the simulation results of this system. Fig. 6(a) shows the three-phase output current, Fig. 6(b) depicts the converter filter output line-to-neutral three-phase voltage, Fig. 6(c), is d- and q-components of the converter output current, Fig. 6(d), is d- and q-components of the converter terminal voltage, Fig. 6(e) depicts the output active and reactive power, and finally, Fig. 6(f) shows the angular frequency generated by the controller. It is seen that the controller tracks the reference active and reactive power with zero steady-state error, and the time constant of the system is about 10 ms, as expected.

Also, Fig. 7 shows the simulation results of the system upon a fault occurrence and phase jump. Initially, the converter injects P=4 MW and Q=2 MVAR into the grid. At t=0.05 s, a 100 ms three-phase fault making the grid voltage 0.2 pu occurs in the system. However, it is seen that the system output power and generated angular frequency have a constant steady-state error during the fault. The reason is in (8), the controllers corresponding to $\Delta\omega$ are just proportional controllers. This prevents creating an accumulative error in the generated frequency, and hence, the output active power. After the fault clearance (t=0.15 s), the line power transferred limit is increased again, and the output active power is recovered. In addition, at t=0.25 s, a 20° phase jump occurs at the grid side voltage. It is seen that the system can maintain stability and inject the reference active and reactive power into the grid after the phase jump occurrence.

3) Comparative Analysis: In this part, the proposed control strategy is compared with PSGFLI and VMDPC. To compare the performance of the LPV-PSGFLI and PSGFLI, both systems are connected to the weak grid with SCR=1.2. Initially, both IBRs inject 1 MW and 1 MVAR to the grid. At t=0.1 s, the active power is increased to 2 MW, and after 100 ms, it is increased to 4 MW. At t=0.3 s, the reactive power is increased to 2 MVAR. Finally, At t=0.4 s, the active power direction is reversed, changing the inverter mode to rectification. Fig. 8 shows the simulation results of this test in which (a) depicts the injected active power and (b) shows the injected reactive power by the LPV-PSGFLI and PSGFLI, respectively. It is observed that LPV-PSGFLI has a constant rise time, while the PSGFLI rise time varies depending on the operating point. Additionally, the PSGFLI cannot perform as a rectifier while LPV-GFLI remains stable and tracks its power references even in the rectification mode. The reason is when the active power direction is reversed, the current direction will change and the loop transfer function L of PSGFLI becomes -L, which adds a phase lag of -180 to the loop transfer function that makes the system unstable. However, the LPV controller designed for the PSGFLI varies depending on the operating point and is able to deal with the IBR mode change.

To compare the performance of the proposed control design with the VMDPC while connected to a weak grid, similar active and reactive reference changes are applied to a system that has the VMDPC control structure. With the VMDPC, the system is unable to work in a weak grid unless the gain of the system and subsequently, its speed, decrease drastically. Fig. 9 shows the simulation results of the VMDPC. Similar to the tests applied to the proposed controller in this study, initially, the IBR injects 1 MW and 1 MVAR. At t=1 s, the active power set-point is changed to 2 MW. At t=3.5 s, the reactive power set-point steps up to 4 MVAR, while the active power remains unchanged. At

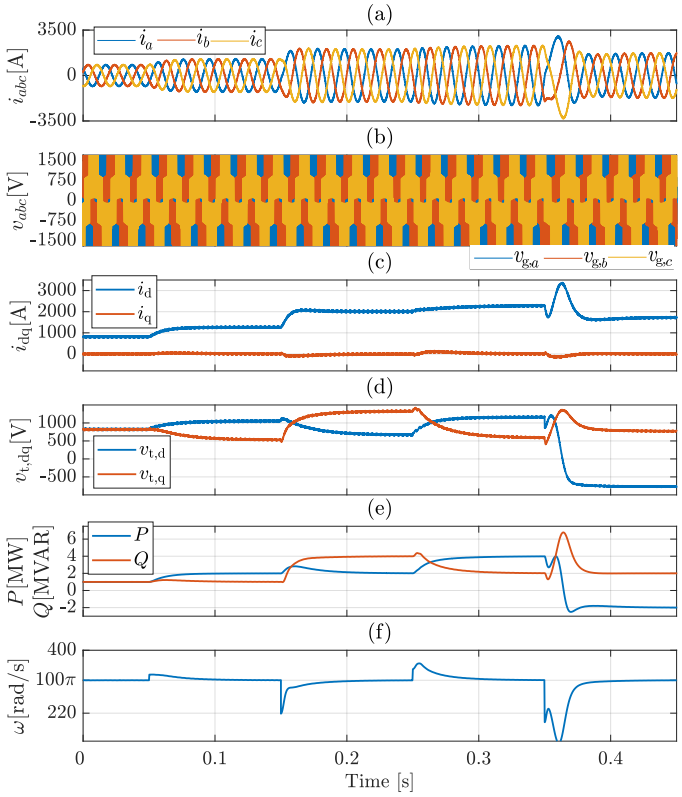

Fig. 6. The simulation results of the system with SCR=1.2 upon various active and reactive power references change: a) the three-phase grid currents (i_{abc}), b) the grid three-phase line-to-neutral voltage, c) the dq-components of the grid current (i_{dq}), d) the dq-components of the terminal voltage ($v_{t,dq}$), e) the injected active and reactive power into the grid, and f) the estimated angular frequency generated by the controller.

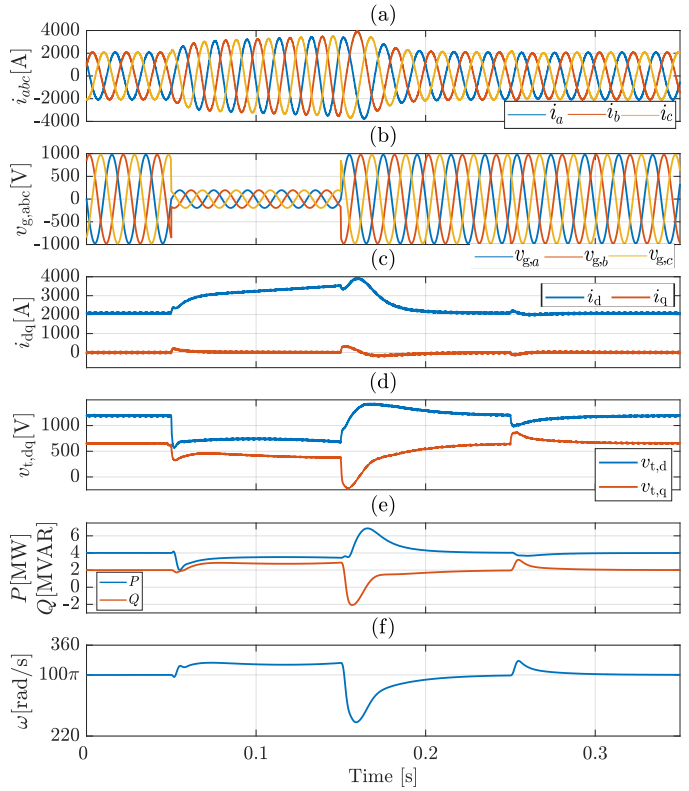

Fig. 7. The simulation results of the system with SCR=1.2 upon a three-phase fault and grid voltage phase jump occurrence: a) the three-phase grid currents (i_{abc}), b) the grid three-phase line-to-neutral voltage, c) the dq-components of the grid current (i_{dq}), d) the dq-components of the terminal voltage ($v_{t,dq}$), e) the injected active and reactive power into the grid, and f) the estimated angular frequency generated by the controller.

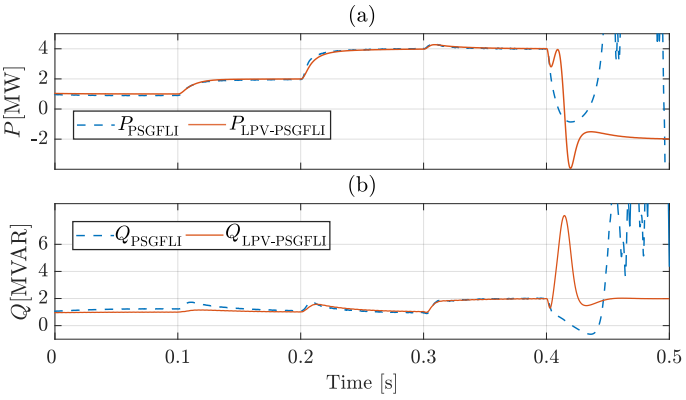

Fig. 8. The simulation results of the comparison between the LPV-PSGFLI and PSGFLI while the IBR is connected to the weak grid with SCR=1.2 upon various active and reactive power reference changes: a) the injected active power into the grid and b) the injected reactive power into the grid.

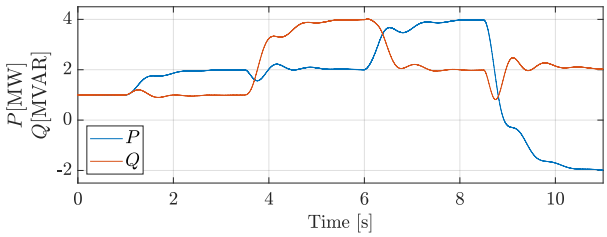

Fig. 9. The simulation results (active and reactive power) of the VMDPC [36], when connected to a very weak grid with SCR=1.2, upon active and reactive power references change.

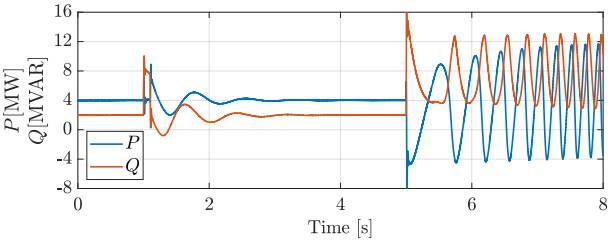

Fig. 10. The simulation results (active and reactive power) of the VMDPC [36], when connected to a very weak grid with SCR=1.2, upon a three-phase grid-side fault and a 20° grid voltage phase jump.

t=6 s, the power factor is changed from 0.44 to 0.9, changing the active and reactive power set-points to 4 MW and 2 MVAR, respectively. Finally, at t=8.5 s, the converter active power set-point is changed to -2 MW, making the converter a rectifier. It is seen that the rise time of the system is about 1 s, which is 100 times slower than the controller proposed in this study. It should be noted that, when connected to a weak grid, the VMDPC becomes unstable if the overall gain of the system increases (to make the system faster).

Additionally, a 100 ms three-phase grid-side fault that causes the grid voltage to drop to 0.2 pu followed by a 20° grid voltage phase jump is applied to the same system using the VMDPC connected to the same weak grid. The simulation result is presented in Fig. 10. At t=1, the three-phase fault takes place and gets clear after 100 ms. It is seen that although the controller can stabilize the system, the settling time is about 1.5 s, which is much slower than the proposed controller performance. Additionally, at t=5 s,

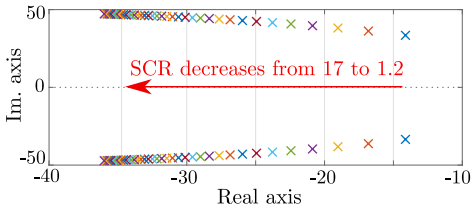

Fig. 11. The eigenvalues of the system while the SCR varies from 17 to 1.2, while the controller is designed based on SCR= 5 and X/R=3.

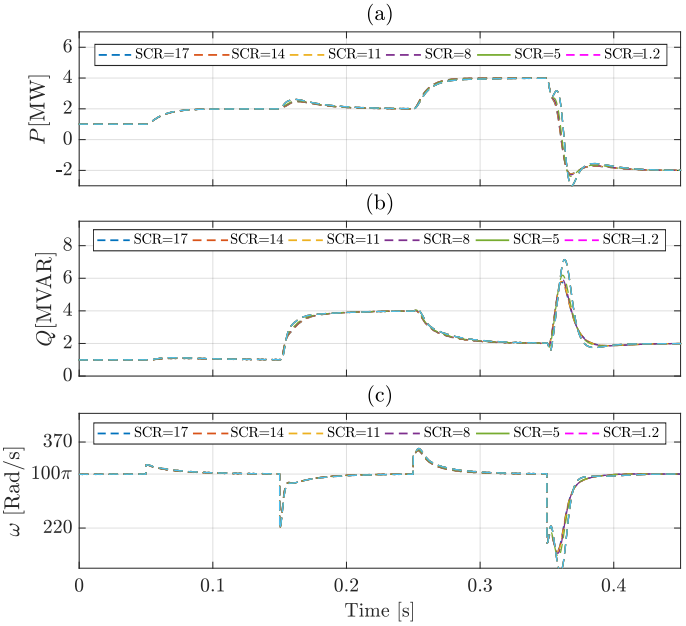

Fig. 12. The simulation results of the system while the SCR varies from 17 to 1.2 with a controller designed based on SCR=5 and X/R=3: a) the injected active power into the grid, b) the injected reactive power into the grid, and c) the estimated angular frequency generated by the controller.

TABLE II
THE PARAMETERS OF THE EXPERIMENTAL SETUP.

Quantity	Value	Comment
L_{f}	14 mH	Inverter Filter Inductance
R_{f}	0.5 Ω	Series Resistance of L_{f}
S_{base}	1 kVA	Inverter Rated Power
v_{g}	100 V	Grid Line-to-Line Voltage (rms)
v_{dc}	300 V	DC Bus Voltage
f_{sw}	20 kHz	PWM Carrier Frequency
f	50 Hz	System Nominal Frequency
f_{filt}	200 Hz	Power Measurement LPF Bandwidth

a 20° phase jump occurs at the grid voltage. It is seen that, contrary to the introduced control method in this study, the VMDPC fails to stabilize the system upon the phase jump.

As conclusion, the LPV controller proposed in this paper has a major advantage compared to the VMDPC while the system is connected to a weak grid. First, the proposed controller is quite faster compared to the VMDPC. Besides, it is seen that in case of severe disturbance occurrence, such as a phase jump, the VMDPC cannot stabilize the system while the proposed LPV controller used for the control structure in [40] rejects the disturbance properly.

4) Robustness Analysis: In this part, the robustness of the proposed controller against grid impedance estimation errors is investigated. To this end, the controller is designed based on a grid with SCR=5 and X/R=3, while the real SCR varies between 17 and 1.2, X/R is kept at 3, and the IBR injects 4 MW and 2 MVAR. Fig. 11 shows the dominant poles of the system when the SCR is decreased from 17 to 1.2 with steps of 0.1. It is seen that the dominant poles are always stable. Besides, similar to the robustness analysis used in [45], to validate the eigenvalue analysis results, time-domain simulations are conducted. Fig. 12 shows the time-domain simulation of the system in the presence of impedance estimation errors. In this test, the SCR is set to 17, 14, 11, 8, 5, and 1.2, while the controller remains unchanged. Similar to the previous tests, k_p is set to 100. Initially, the converter injects 1 MW and 1 MVAR of active and reactive power, respectively. At t=0.05 s, the active power set-point is changed to 2 MW. At t=0.15 s, the reactive power set-point steps up to 4 MVAR, while the active power remains unchanged. At t=0.25 s, the power factor is changed from 0.44 to 0.9, changing the active and reactive power set-points to 4 MW and 2 MVAR, respectively. Finally, at t=0.35 s, the converter active power set-point is changed to -2 MW, making the converter work as a rectifier. Fig. 12(a) shows the active power, Fig. 12(b) is the reactive power, and Fig. 12(c) depicts the angular frequency. It is seen that the system remains stable, although there are discrepancies in the estimated grid inductance and resistance, which is used in the controller.

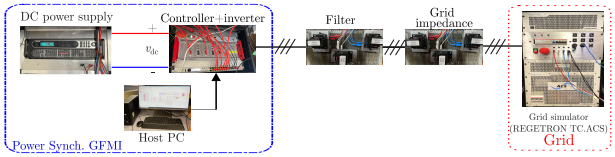

Fig. 13. The experimental setup.

B. Experimental Results

To experimentally evaluate the performance of the proposed controller and to validate the simulation results, an experimental platform based on Imperix B-Box and Regatron AC Power Supply is designed, which is shown in Fig. 13. The corresponding control structures are implemented in Matlab/Simulink, and the control interface is performed via Imperix ACG BB Control software. Table II shows the system parameters. Additionally, the inner current controller gain is set to 2500. Additionally, the parameter k_p is set to 25 in all tests, making the time constant of the system equal to 40 ms. In these tests, the performance of the controller for active power, reactive power, and power factor changes is evaluated. Additionally, the IBR behavior upon fault recovery in the presence of current saturation is evaluated.

1) Strong grid (SCR=31): In the first test, the grid inductance and resistance are set to 1 mH and 0.03 Ω, respectively, making the SCR=31. Initially, the inverter injects no active or reactive power into the grid. At t=0.1 s, the reactive power reference is changed to 800 VAR. At t=0.35 s, the active power set-point is changed to 600 W. Finally, at t=0.6 s, the power factor is changed from 0.6 to 0.8, while the apparent power is kept at 1 pu. Fig. 14 shows the experimental results of this test. Fig. 14(a) is the three-phase injected currents, Fig. 14(b) is the three-phase grid line-to-neutral voltages, Fig. 14(c) shows the active and reactive power, Fig. 14(d) depicts the d and q-components of the injected current, as well as the generated i_{d} reference value by the controller, Fig. 14(e) depicts the d and q-components of the terminal voltage, and finally, Fig. 14(f) shows the angular frequency estimated by the controller. It is seen that the system time constant is about 40 ms, and the controller regulates the P and Q upon changes in their references.

2) Weak grid (SCR=1.9): In the second test, the grid inductance and resistance are set to 16 mH and 0.53 Ω, respectively, making

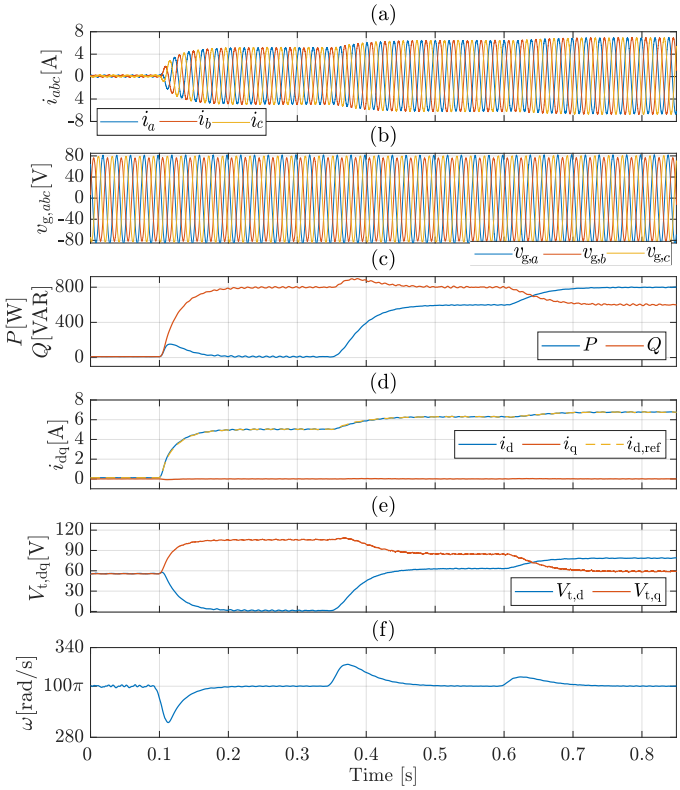

Fig. 14. The experimental results of the LPV-PSGFLI while connected to a strong grid with SCR=31 showing the zero-start, as well as active and reactive reference changes: a) the three-phase grid currents (i_{abc}), b) the grid three-phase line-to-neutral voltage, c) the injected active and reactive power into the grid, d) the dq-components of the grid current (i_{dq}) and $i_{d,ref}$, e) the dq-components of the terminal voltage ($v_{t,dq}$), and f) the estimated angular frequency generated by the controller.

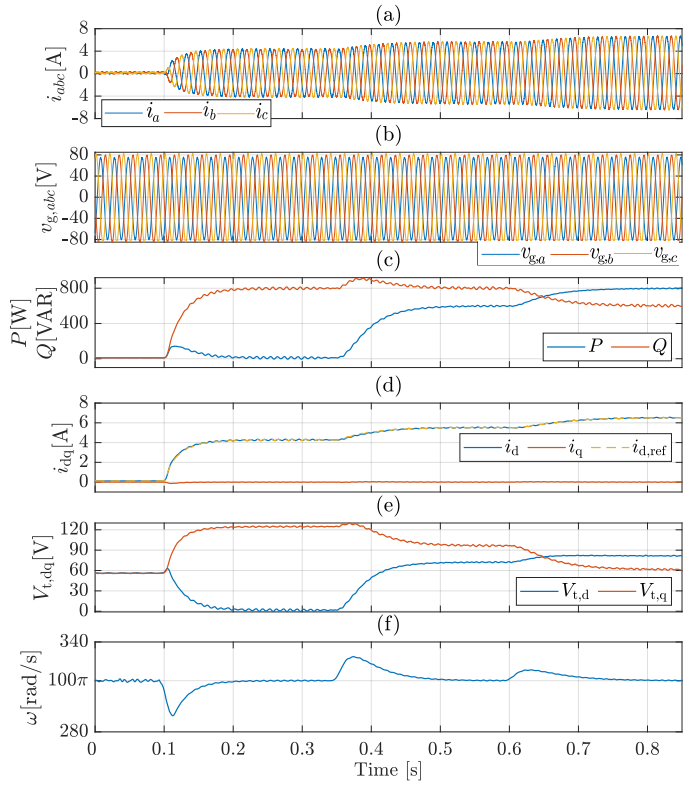

Fig. 15. The experimental results of the LPV-PSGFLI while connected to a weak grid with SCR= 1.9 showing the zero-start, as well as active and reactive reference changes: a) the three-phase grid currents (i_{abc}), b) the grid three-phase line-to-neutral voltage, c) the injected active and reactive power into the grid, d) the dq-components of the grid current (i_{dq}) and $i_{d,ref}$, e) the dq-components of the terminal voltage ($v_{t,dq}$), and f) the estimated angular frequency generated by the controller.

the SCR=1.9. Initially, the inverter injects no active or reactive power into the grid. At t=0.1 s, the reactive power reference is changed to 800 VAR. At t=0.35 s, the active power set-point is changed to 600 W. Finally, at t=0.6 s, the power factor is changed from 0.6 to 0.8, while the apparent power is kept at 1 pu. Fig. 15 shows the experimental results of this test. Fig. 15(a) is the three-phase injected currents, Fig. 15(b) is the three-phase grid line-to-neutral voltages, Fig. 15(c) shows the active and reactive power, Fig. 15(d) depicts the d and q-components of the injected current, as well as the generated i_d reference value by the controller, Fig. 14(e) depicts the d and q-components of the terminal voltage, and finally, Fig. 15(f) shows the angular frequency estimated by the controller. It is seen that the system time constant is about 40 ms, and the controller regulates the P and Q upon changes in their references.

3) Fault Occurrence: In the third test, the inverter is connected to the introduced strong system with SCR =31. Initially, the IBR injects 800 W and 600 VAR to the grid. At t=0.08 s, a grid-side three-phase fault causing a 0.5 pu voltage deep occurs for 100 ms. At t=0.18, the fault is cleared. Note that the inverter output current is limited to 8 A, and an anti-windup mechanism is employed in the control structure to avoid instability due to saturation. Fig. 16 shows the experimental results of this test in which (a) is the three-phase output currents, (b) is the three-phase grid line-to-neutral voltages, (c) is the active and reactive power, (d) depicts the injected current d and q-components of the injected current, and (e) shows the angular frequency estimated by the controller. It is observed that during the fault, the output current is saturated to 8 A. After the fault is cleared, the controller is able to track the references, and the system is recovered.

Based on the results shown in the simulation and experimental tests, it is seen that the proposed controller rectifies the issues present in the control design method of [40]. The proposed controller has a constant bandwidth for different operating points and can perform as a rectifier with no need to modify the controller. Besides, contrary to the method in [40], the proposed controller has a parametric, easy-to-design structure.

V. Conclusions

This paper proposes an LPV loop-shaping controller for PS-GFLIs. IBRs enjoying this structure do not have stability issues while connected to very strong or very weak grids; also, it is shown that using this controller, the performance of the system does not rely on the operating point, i.e., it adapts its gains such that it has a constant rise time while working in different operating points. Additionally, the designed controller allows the system to work as a bidirectional converter. Besides, the proposed controller shapes the system open-loop transfer function such that IBR output active and reactive power are decoupled, and the rise time of the system can easily be tuned by changing the system open-loop gain. Moreover, it is mathematically shown that the system is robust despite the discrepancies that might occur in grid inductance and resistance estimation. Finally, the performance of the proposed control structure is validated via simulation and experimental tests.

As a continuation of this work, the transient and small-signal stability analyses of a grid-connected LPV-PSGFLI equipped with the proposed controller will be conducted, and the impact of asymmetrical faults on the proposed controller will be studied.

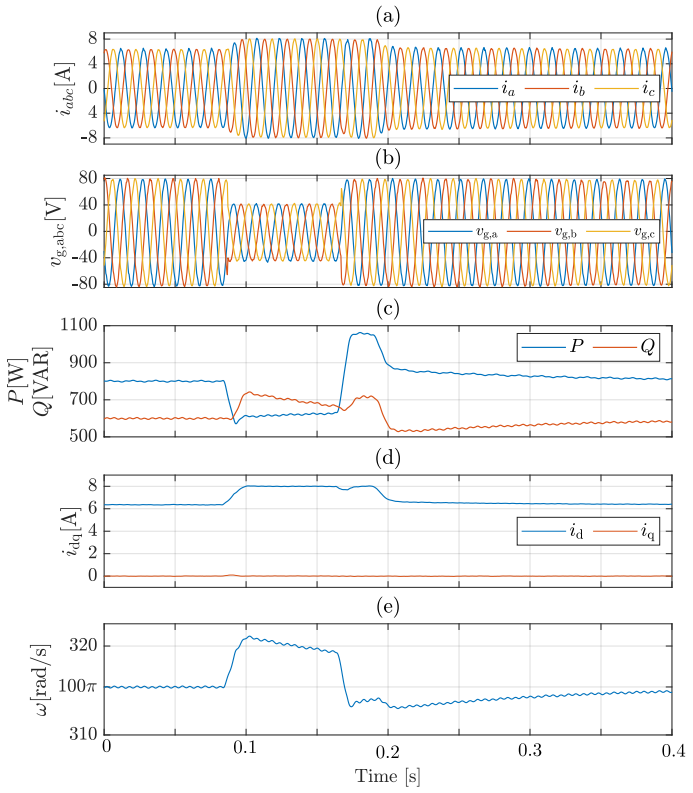

Fig. 16. The experimental results of the system while the IBR is connected to the strong grid with SCR=31 upon a 100 ms fault occurrence: a) the three-phase grid currents (i_{abc}), b) the grid three-phase line-to-neutral voltage, c) the injected active and reactive power into the grid, d) the dq-components of the grid current (i_{dq}), and e) the estimated angular frequency generated by the controller.

REFERENCES

[1] K. E. et al., *Connection of Wind Farms to Weak AC Networks*. WG B4.62.671, CIGRE, 2016.

[2] F. Blaabjerg, R. Teodorescu, M. Liserre, and A. V. Timbus, "Overview of Control and Grid Synchronization for Distributed Power Generation Systems," *IEEE Transactions on Industrial Electronics*, vol. 53, no. 5, pp. 1398–1409, Oct. 2006.

[3] R. H. Lasseter, Z. Chen, and D. Pattabiraman, "Grid-Forming Inverters: A Critical Asset for the Power Grid," *IEEE Journal of Emerging and Selected Topics in Power Electronics*, vol. 8, no. 2, pp. 925–935, Dec. 2020.

[4] T. Xia, X. Zhang, G. Tan, and Y. Liu, "All-Pass-Filter-Based PLL for Single-Phase Grid-Connected Converters Under Distorted Grid Conditions," *IEEE Access*, vol. 8, pp. 106 226–106 233, June 2020.

[5] A. Luna, J. Rocabert, J. I. Candela, J. R. Hermoso, R. Teodorescu, F. Blaabjerg, and P. Rodríguez, "Grid Voltage Synchronization for Distributed Generation Systems Under Grid Fault Conditions," *IEEE Transactions on Industry Applications*, vol. 51, no. 4, pp. 3414–3425, Jan. 2015.

[6] B. Bahrani, S. Kenzelmann, and A. Rufer, "Multivariable-PI-based *dq* current control of voltage source converters with superior axis decoupling capability," *IEEE Transactions on Industrial Electronics*, vol. 58, no. 7, pp. 3016–3026, Aug. 2010.

[7] B. Bahrani, M. Vasiladiotis, and A. Rufer, "High-order vector control of grid-connected voltage-source converters with LCL-filters," *IEEE Transactions on Industrial Electronics*, vol. 61, no. 6, pp. 2767–2775, Aug. 2013.

[8] X. Wang, M. G. Taul, H. Wu, Y. Liao, F. Blaabjerg, and L. Harnefors, "Grid-synchronization stability of converter-based resources—an overview," *IEEE Open Journal of Industry Applications*, vol. 1, pp. 115–134, Aug. 2020.

[9] J. Machowski, Z. Lubosny, J. W. Bialek, and J. R. Bumby, *Power system dynamics: stability and control*. John Wiley & Sons, 2020.

[10] L. Zhang, L. Harnefors, and H.-P. Nee, "Power-synchronization control of grid-connected voltage-source converters," *IEEE Transactions on Power systems*, vol. 25, no. 2, pp. 809–820, Nov. 2009.

[11] X. Meng, J. Liu, and Z. Liu, "A generalized droop control for grid-supporting inverter based on comparison between traditional droop control and virtual synchronous generator control," *IEEE Transactions on Power Electronics*, vol. 34, no. 6, pp. 5416–5438, Sept. 2019.

[12] H. Wu and X. Wang, "Design-oriented transient stability analysis of PLL-synchronized voltage-source converters," *IEEE Transactions on Power Electronics*, vol. 35, no. 4, pp. 3573–3589, Aug. 2019.

[13] X. Wang and F. Blaabjerg, "Harmonic stability in power electronic-based power systems: concept, modeling, and analysis," *IEEE Transactions on Smart Grid*, vol. 10, no. 3, pp. 2858–2870, Mar. 2018.

[14] M. G. Taul, X. Wang, P. Davari, and F. Blaabjerg, "Systematic Approach for Transient Stability Evaluation of Grid-tied Converters During Power System Faults," in *IEEE Energy Conversion Congress and Exposition (ECCE)*, 2019, pp. 5191–5198.

[15] J. Zhao, M. Huang, H. Yan, C. K. Tse, and X. Zha, "Nonlinear and transient stability analysis of phase-locked loops in grid-connected converters," *IEEE Transactions on Power Electronics*, vol. 36, no. 1, pp. 1018–1029, June 2021.

[16] H. Wu and X. Wang, "Transient angle stability analysis of grid-connected converters with the first-order active power loop," in *Applied Power Electronics Conference and Exposition (APEC)*. IEEE, 2018, pp. 3011–3016.

[17] H. Geng, L. Liu, and R. Li, "Synchronization and reactive current support of PMSG-based wind farm during severe grid fault," *IEEE Transactions on Sustainable Energy*, vol. 9, no. 4, pp. 1596–1604, Feb. 2018.

[18] F. Andrade, K. Kampouropoulos, L. Romeral, J. C. Vasquez, and J. M. Guerrero, "Study of large-signal stability of an inverter-based generator using a Lyapunov function," in *IECON 2014 - 40th Annual Conference of the IEEE Industrial Electronics Society*, 2014, pp. 1840–1846.

[19] M. Z. Mansour, S. P. Me, S. Hadavi, B. Badrazadeh, A. Karimi, and B. Bahrani, "Nonlinear Transient Stability Analysis of Phase-Locked Loop Based Grid-Following Voltage Source Converters Using Lyapunov's Direct Method," *IEEE Journal of Emerging and Selected Topics in Power Electronics*, Feb. 2021, doi: 10.1109/TIE.2016.2619660.

[20] Y. Liao, X. Wang, F. Liu, K. Xin, and Y. Liu, "Sub-synchronous control interaction in grid-forming VSCs with droop control," in *2019 4th IEEE Workshop on the Electronic Grid (eGRID)*. IEEE, 2019, pp. 1–6.

[21] S. Wang, Z. Liu, J. Liu, D. Boroyevich, and R. Burgos, "Small-signal modeling and stability prediction of parallel droop-controlled inverters based on terminal characteristics of individual inverters," *IEEE Transactions on Power Electronics*, vol. 35, no. 1, pp. 1045–1063, May 2019.

[22] H. Wu and X. Wang, "Design-oriented transient stability analysis of grid-connected converters with power synchronization control," *IEEE Transactions on Industrial Electronics*, vol. 66, no. 8, pp. 6473–6482, Oct. 2018.

[23] D. Pan, X. Wang, F. Liu, and R. Shi, "Transient stability of voltage-source converters with grid-forming control: a design-oriented study," *IEEE Journal of Emerging and Selected Topics in Power Electronics*, vol. 8, no. 2, pp. 1019–1033, Oct. 2019.

[24] G. Denis, T. Prevost, P. Panciatici, X. Kestelyn, F. Colas, and X. Guillaud, "Improving robustness against grid stiffness, with internal control of an ac voltage-controlled vsc." in *2016 IEEE Power and Energy Society General Meeting (PESGM)*. IEEE, 2016.

[25] G. Li, Y. Chen, A. Luo, Z. He, H. Wang, Z. Zhu, W. Wu, and L. Zhou, "Analysis and mitigation of subsynchronous resonance in series-compensated grid-connected system controlled by a virtual synchronous generator," *IEEE Transactions on Power Electronics*, vol. 35, no. 10, pp. 11 096–11 107, Mar. 2020.

[26] M. G. Taul, X. Wang, P. Davari, and F. Blaabjerg, "Current limiting control with enhanced dynamics of grid-forming converters during fault conditions," *IEEE Journal of Emerging and Selected Topics in Power Electronics*, vol. 8, no. 2, pp. 1062–1073, July 2019.

[27] O. Mo, S. D'Arco, and J. A. Suul, "Evaluation of virtual synchronous machines with dynamic or quasi-stationary machine models," *IEEE Transactions on Industrial Electronics*, vol. 64, no. 7, pp. 5952–5962, Dec. 2016.

[28] M. Malinowski, M. Jasinski, and M. P. Kazmierkowski, "Simple direct power control of three-phase PWM rectifier using space-vector modulation (DPC-SVM)," *IEEE Transactions on Industrial Electronics*, vol. 51, no. 2, pp. 447–454, Apr. 2004.

[29] T. Noguchi, H. Tomiki, S. Kondo, and I. Takahashi, "Direct power control of PWM converter without power-source voltage sensors," *IEEE transactions on industry applications*, vol. 34, no. 3, pp. 473–479, May 1998.

[30] A. Bouafia, J. Gaubert, and F. Krim, "Predictive direct power control of three-phase pulse-width modulation (PWM) rectifier using space-vector modulation (SVM)," *IEEE Transactions on Power Electronics*, vol. 25, no. 1, pp. 228–236, Aug. 2009.

[31] D. Zhi and L. Xu, "Direct power control of DFIG with constant switching frequency and improved transient performance," *IEEE Transactions on Energy Conversion*, vol. 22, no. 1, pp. 110–118, Feb. 2007.

[32] S. Vazquez, J. A. Sanchez, J. M. Carrasco, J. I. Leon, and E. Galvan, "A model-based direct power control for three-phase power converters," *IEEE Transactions on Industrial Electronics*, vol. 55, no. 4, pp. 1647–1657, Apr. 2008.

[33] J. Hu, L. Shang, Y. He, and Z. Zhu, "Direct active and reactive power regulation of grid-connected dc/ac converters using sliding mode control approach," *IEEE Transactions on Power Electronics*, vol. 26, no. 1, pp. 210–222, July 2010.

[34] Y. Gui, G. H. Lee, C. Kim, and C. C. Chung, "Direct power control of grid connected voltage source inverters using port-controlled hamiltonian system," *International Journal of Control, Automation and Systems*, vol. 15, no. 5, pp. 2053–2062, Sept. 2017.

[35] L. Harnefors, J. Kukkola, M. Routimo, M. Hinkkanen, and X. Wang, "A universal controller for grid-connected voltage-source converters," *IEEE Journal of Emerging and Selected Topics in Power Electronics*, vol. 9, no. 5, pp. 5761–5770, Nov. 2021.

[36] Y. Gui, X. Wang, F. Blaabjerg, and D. Pan, "Control of grid-connected voltage-source converters: the relationship between direct-power control and vector-current control," *IEEE Industrial Electronics Magazine*, vol. 13, no. 2, pp. 31–40, June 2019.

[37] Y. Gui, X. Wang, and F. Blaabjerg, "Vector current control derived from direct power control for grid-connected inverters," *IEEE Transactions on Power Electronics*, vol. 34, no. 9, pp. 9224–9235, Nov. 2019.

[38] Y. Gui, X. Wang, H. Wu, and F. Blaabjerg, "Voltage-modulated direct power control for a weak grid-connected voltage source inverters," *IEEE Transactions on Power Electronics*, vol. 34, no. 11, pp. 11 383–11 395, Feb. 2019.

[39] S. Milad Hoseinizadeh, S. Ouni, H. Karimi, M. Karimi-Ghartemani, and K. L. Lian, "Comparison of PLL-based and PLL-less vector current controllers," *IEEE Journal of Emerging and Selected Topics in Power Electronics*, Mar. 2021, doi: 10.1109/JESTPE.2021.3066512.

[40] B. Bahrani, "Power-synchronized grid following inverter without a phase-locked loop," *IEEE Access*, vol. 9, pp. 112 163–112 176, Aug. 2021.

[41] J. Mohammadpour and C. W. Scherer, *Control of linear parameter varying systems with applications*. Springer Science & Business Media, 2012.

[42] S. Jayalath and M. Hanif, "Generalized LCL-filter design algorithm for grid-connected voltage-source inverter," *IEEE Transactions on Industrial Electronics*, vol. 64, no. 3, pp. 1905–1915, Oct. 2016.

[43] J. H. Suárez, H. M. Gomes, A. J. Sguarezi Filho, D. A. Fernandes, and F. F. Costa, "Grid impedance estimation for grid-tie inverters based on positive sequence estimator and morphological filter," *Electrical Engineering*, p. 1195–1205, Feb. 2020.

[44] N. Mohammed, M. Ciobotaru, and G. Town, "Fundamental grid impedance estimation using grid-connected inverters: a comparison of two frequency-based estimation techniques," *IET Power Electronics*, vol. 13, no. 13, pp. 2730–2741, Oct. 2020.

[45] T. Qoria, E. Rokrok, A. Bruyere, B. François, and X. Guillaud, "A PLL-free grid-forming control with decoupled functionalities for high-power transmission system applications," *IEEE Access*, vol. 8, pp. 197 363–197 378, Oct. 2020.

Milad Zarif Mansour (S'19) received the B.Sc. degree from the University of Tehran, Tehran, Iran, and the M.Sc. degree from Sharif University of Technology, Tehran, Iran, both in electrical engineering, in 2016 and 2018, respectively. Since 2019, he has been pursuing a Ph.D. degree at Monash University, Melbourne, Australia. His research interests include grid integration of renewable energy resources, control of power electronic devices, and applications of power electronics in power systems.

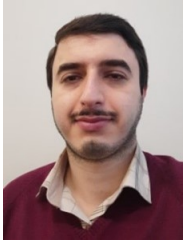

Mohammad Hasan Ravanji Member, IEEE, received his B.Sc., M.Sc. and Ph.D. degrees all in electrical power engineering from Sharif University of Technology (SUT), Tehran, Iran, in 2012, 2014, and 2020, respectively. He was a visiting student with the University of Waterloo, Waterloo, ON, Canada from Oct. 2017 to April 2018. Further, he was with the Iran Grid Management Company (IGMC), Tehran, Iran, as a researcher in their system planning and dynamic studies group from Feb. 2019 to July 2020. He is currently a post-doctoral research fellow at Monash University, Melbourne, Australia. His current research interests include power system stability, renewable energy systems and the application of grid forming and grid following inverters in weak power grids.

Alireza Karimi received the Ph.D. degree in 1997 from Institut National Polytechnique de Grenoble, Grenoble, France. He was an Assistant Professor with the Department of Electrical Engineering, Sharif University of Technology, Tehran, Iran, from 1998 to 2000. Then, he Joined then Ecole Polytechnique Federale de Lausanne (EPFL) in Switzerland and is currently a Professor of automatic control in the Mechanical Engineering Institute of EPFL. Prof. Karimi is the head of "data-driven modelling and control" group in Automatic Control Laboratory and his research interests include data-driven controller design approaches with applications to power grids and mechatronic systems. Prof. Karimi was an Associate Editor of European Journal of Control from 2004 to 2013 and is a member of the conference editorial board of IEEE control systems society since 2018.

Behrooz Bahrani (M'13–SM'19) received the B.Sc. degree from Sharif University of Technology, Tehran, Iran, the M.Sc. degree from the University of Toronto, Toronto, ON, Canada, and the PhD degree from the Ecole Polytechnique Fédérale de Lausanne (EPFL), Lausanne, Switzerland, all in electrical engineering, in 2006, 2008, and 2012, respectively. From September 2012 to September 2015, he was a Postdoctoral Fellow at several institutions including EPFL, Purdue University, West Lafayette, IN, USA, Georgia Institute of Technology, Atlanta, GA, USA, and the Technical University of Munich, Munich, Germany. Since 2015, he has been with Monash University, Clayton, Australia, where currently, he is a Senior Lecturer and the Director of the Grid Innovation Hub. His research interests include control of power electronics systems, applications of power electronics in power and traction systems, and grid integration of renewable energy resources.